Measurement of SST and SSS Using Frequencies in the Range 0.3 – 2.0 GHz

David M. Le Vine[1] and Emmanuel P. Dinnat[1,2]

[1]Goddard Space Flight Center, Greenbelt, MD 20771 USA

[2]Center of Excellence in Earth Systems Modeling and Observations, Chapman University, Orange, CA 92866 USA

Corresponding author: David M. Le Vine (david.m.levine@nasa.gov)

Key Points:

- Measurement of sea surface temperature is possible as part of low frequency wideband remote sensing of the cryosphere.
- Measurement of SST to support wideband remote sensing of sea surface salinity is possible.

Abstract

Wide bandwidth radiometer systems that make measurements at multiple frequencies in the range 300 MHz to 2 GHz have been proposed to address parameters important for understanding issues in the cryosphere associated with climate change such as ice sheet thickness and temperature. It is also possible with such a system to retrieve sea surface salinity (SSS) which is important for understanding the impact of climate change on ocean circulation at high latitude. In contemporary sensors for retrieving SSS, such as SMOS and SMAP, sea surface temperature (SST), another parameter important for understanding ocean circulation and necessary in the retrieval of salinity, is treated as an ancillary parameter obtained from an independent source. However, both SSS and SST have peaks in sensitivity below 1 GHz; and it has been shown that measurements at multiple frequencies in this portion of the spectrum can take advantage of this peak in sensitivity to improve the accuracy of the retrieval of SSS. In this manuscript it will be shown that there is also the potential to retrieve SST and, in cold water, the possibility for improved accuracy over existing retrievals.

1 Introduction

Modern remote sensing radiometers in space at the long wavelength end of the microwave spectrum, such as flown on SMOS [Kerr et al, 2010] and SMAP [Entekhabi et al, 2010,2014], operate in the narrow 27 MHz of spectrum at 1.413 GHz protected for passive use. Operating in protected spectrum is necessary to detect natural thermal emission from the surface and avoid being overwhelmed by interference from manmade sources of radiation. These radiometers have demonstrated remote sensing of sea surface salinity (SSS) [Dinnat et al, 2019; Kao et al, 2018] and soil moisture [Bindlish et al, 2019; Chan et al, 2018] and the potential for monitoring ice thickness [Johnson et al, 2021]. However, contemporary research suggests that in polar regions, where radio frequency interference (RFI) is less problematic it may be possible to operate over a wider bandwidth [Andrews et al, 2021]. In particular, wide bandwidth radiometers that measure

at multiple frequencies in the range of 0.3 – 2.0 GHz have the potential for profiling ice sheet temperature [Yardim et al, 2022], measuring ice thickness [Jezek et al, 2019] and improving the retrieval of SSS especially in cold water [Le Vine and Dinnat, 2022; Vinogradova et al, 2019]. These are parameters of increasing importance for understanding the potential impact of climate change. The success of the digital processing and sophisticated RFI detection algorithms demonstrated by SMAP [Piepmeier et al, 2014; de Matthaeis et al 2021] suggest that operating in unprotected spectrum in sparsely populated areas of the world such as the Arctic is realistic, especially if one is not restricted to a single fixed frequency.

In the case of SSS, recent research has shown that making several measurements simultaneously over the frequency range 0.3 - 2.0 GHz could improve the accuracy of the retrieved salinity [Le Vine and Dinnat, 2022]. This is especially true in cold water where the retrieval at 1.4 GHz by radiometers such as Aquarius and SMAP is noisy relative to retrievals over the open ocean [Dinnat et al, 2019]; and cold water is particularly important because it is associated with regions that are important for understanding the impact of climate change and melting ice on ocean circulation [Rahmstorf, 2006; Duncan et al. 2020]. One of the reasons that a radiometer operating in this frequency range improves the retrieval of SSS is that the peak sensitivity to SSS lies below 1 GHz; and it moves with water temperature toward lower frequencies as the water temperature decreases. This is illustrated in Fig. 1 (left) which shows the sensitivity of brightness temperatures, TB, to changes in salinity (i.e. ∂TB/∂SSS) as function of frequency for several values of water temperature. A single measurement in the protected band at 1.4 GHz (red arrow) has sensitivity well below the peak, especially in cold water (black curve). It is shown in [Le Vine and Dinnat, 2022] that a simple average of measurements uniformly spaced over the interval 0.3 – 2.0 GHz can improve the retrieval of SSS especially in cold water compared to a single measurement at 1.4 GHz as is currently done.

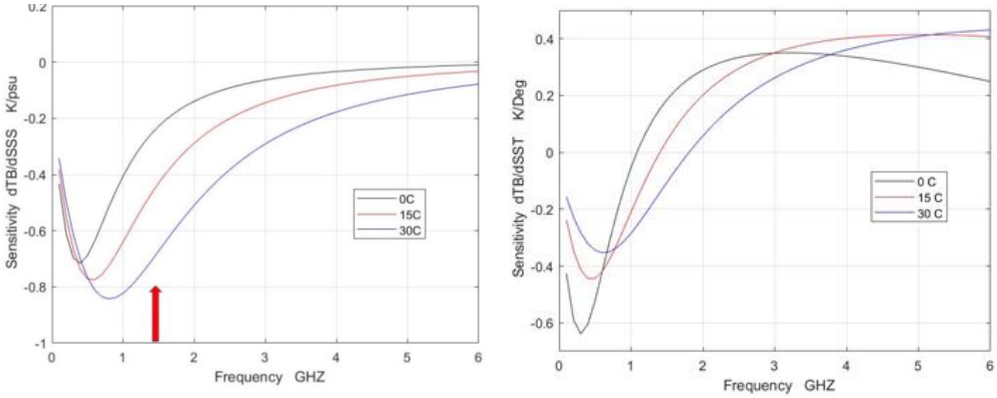

Figure 1: Sensitivity of brightness temperature to salinity (left) and to temperature (right) as a function of frequency for temperatures of (black) 0, (red) 15 and (blue) 30 deg C. The curves are for nadir incidence, SSS = 35 psu and a flat surface (wind speed is 0 m/s). The scales are the same but with an offset zero to show the curves side by side.

The sensitivity to SST also has a peak below 1 GHz with characteristics very similar to the peak in SSS. This is illustrated in the right panel of Fig. 1 which shows the sensitivity of brightness temperatures, TB, to changes in SST (i.e. ∂TB/∂SSST) as function of frequency for several values of SST. These curves are for nadir for SSS = 35 psu and SST = 0, 15 and 30 deg C. The behavior is similar off nadir [Le Vine and Dinnat, 2020] although the values depend on polarization (the peaks below 1 GHz are larger at vertical polarization than at horizontal polarization with nadir in between). As in the case of SSS, the frequency range 0.3 – 2.0 GHz includes the peak in sensitivity to SST over a wide range of water temperature. This paper examines the possibility of taking advantage of the peaks in sensitivity in SST to retrieve SST using measurements at several frequencies spanning this frequency range to capture the peaks as was done in the case of SSS. The curves for ∂TB/∂SSS and ∂TB/∂SST are similar for frequencies below 1 GHz which suggests that the approach for improving SSS [Le Vine and Dinnat, 2022] will also work for SST. However, at higher frequency the two sensitivity curves are much different: the sensitivity to SSS (Fig. 1 left) decreases monotonically toward zero and is almost negligible above a few GHz, but the sensitivity to SST (Fig. 1 right) changes sign in the vicinity of 1-2 GHz and has another peak at frequencies in the range of 5-8 GHz (depending on SST). This change of sign and the existence of a zero for the sensitivity in between complicates the retrieval, as will be shown below.

2 Approach

The starting point in this analysis is an idealized radiometer system. It is assumed that the radiometer is calibrated with no systematic errors and that the retrieval takes into account all issues and is error free. The retrieval is ideal in the sense that if one puts in the correct ancillary information, the retrieval yields the correct values of SSS or SST. It is assumed that SST is a function of three variables, the measured brightness temperature, TB, ocean salinity, SSS, and wind speed, WS, which is a surrogate for the effect of surface roughness and foam in the retrieval. That is, it is assumed that SST = SST(TB, SSS, WS). The retrieval is ideal in the sense that if the correct values of TB, SSS and WS are applied then the correct value of SST is retrieved.

The feasibility of retrieving SST is evaluated by examining the effect of random errors in the input variables. The effect of random error in the input is computed by expanding the retrieved SST in a Taylor series about the error-free value as a function of the error in the input variables, TB, SSS and WS. Only random error is considered. Systematic error such as calibration bias, or bias in the retrieval algorithm are not included. Keeping the first term in the Taylor series

(i.e., linear in the error variables, ΔTB, ΔSSS and ΔWS) yields the following expression for the deviation, ΔSST, from the ideal value, SST0:

$$SST(TB, SSS, WS) = SST0 + \Delta SST \quad (1a)$$

$$\Delta SST = \{ \Delta TB - (\partial TB/\partial SSS)\ \Delta SSS - (\partial TB/\partial WS)\ \Delta WS \} / (\partial TB/\partial SST) \quad (1b)$$

By assumption (no systematic error) the error terms are zero mean. It is also assumed that they are independent. Consequently:

$$< \Delta SST > = 0 \quad (2a)$$

$$<\Delta SST^2> = \{<\Delta TB^2> + (\partial TB/\partial SSS)^2 <\Delta SSS^2> + (\partial TB/\partial WS)^2 <\Delta WS^2> \} / (\partial TB/\partial SST)^2 \quad (2b)$$

Here <•> denotes the ensemble average. The square root of the second moment (Eqn 2b) is, in this case, the standard deviation, STD, of the error and will be denoted by, σ_{SST}. The STD will be used as a metric for the feasibility of retrieving SST. In particular, to be a feasible retrieval, applying input variables with reasonable error standard deviation should yield an σ_{SST} consistent with the current state of the art in microwave remote sensing of SST (e.g. about 0.5 ^{o}C [Gentemann and Hilburn, 2015; Nielsen-Englyst et al. 2018; Pearson et al, 2019]). The first step in the analysis is to compute the error standard deviation, σ_{SST}, as a function of frequency for a reasonable range of input parameters and their associated error. The second step in the analysis is to examine the potential for improvement over a measurement at a single frequency using the multiple frequencies of a wide bandwidth radiometer.

3 Results

3.1 Error STD as a function of frequency

To evaluate σ_{SST}, the derivatives of brightness temperature with respect to SSS, SST and WS that appear in Eqn 2b are needed. Examples are shown in Fig. 1 for $\partial TB/\partial SSS$ and $\partial TB/\partial SST$. These curves have been derived assuming zero wind speed and using the definition for emissivity for an ideal flat surface (e.g. eqn 5 in [Meissner Wentz, Ricciardulli, 2014]) together with the model for the dielectric constant of sea water based on measurements at The George Washington University [Zhou et al, 2021]. Using the flat surface (WS = 0) for computing these two derivatives is based on data from Aquarius and SMAP at 1.4 GHz and on emissivity models which suggests that the effect of wind speed on these two derivatives is relatively small in this frequency range [Dinnat et al., 2003; Meissner et al. 2018]. An analysis supporting this conclusion is presented in Appendix A. Well established analytical expressions in closed form exist for the emissivity in the case of the flat surface (i.e., Eqn 5 in [Meissner,Wentz, Ricciardulli, 2014]) which makes them easy to incorporate into the computations. The examples of these derivatives shown in Fig. 1 are for nadir incidence. Examples for incidence angles of 40 degrees including the variation with SSS can be found in [Le Vine and Dinnat, 2020] and [Le Vine and Dinnat, 2022]. The examples in [Le Vine and Dinnat, 2020] use the Klein-Swift model [Klein and Swift, 1977] for the dielectric constant of sea water which until relatively recently has been the standard for modelling emission from the ocean. However, this model is known to result in relatively large errors in the retrieval of SSS at very low temperatures [Dinnat et al,

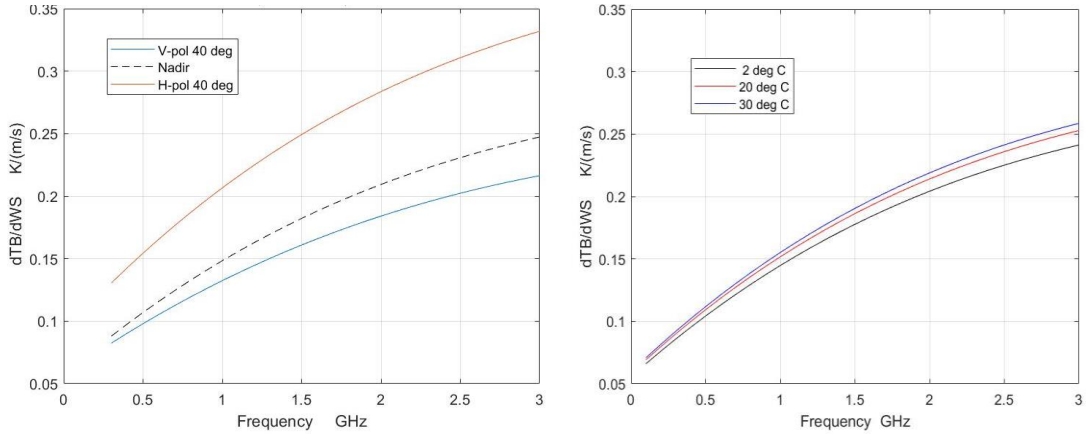

Figure 2: Sensitivity of brightness temperature to wind speed, ∂TB/∂WS, as a function of frequency. Left: Dependence on incidence angle and polarization with examples for nadir = 0 degrees (black dashed) and 40 degrees (orange & blue) for SST = 20 ºC; Right: Dependence on SST for nadir incidence with examples at temperatures of (blue) 2 ºC, (red) 20 ºC and (black) 30 ºC. In both cases WS = 7 m/s and SSS = 35 psu.

2019] and new models have been proposed for application at L-band [Zhou et al, 2021; Boutin et al, 2021, Meissner and Wentz, 2012, 2004] which do not exhibit this problem. In the analysis presented in this manuscript, we elected to use the model of Zhou et al [2021] because it is based on laboratory measurements of the dielectric constant at l.4 GHz and is similar to the model of Klein-Swift [1977] without the issue at low temperatures. However, the choice of the model for the dielectric constant has a minor effect on the kind of analysis being done here [Le Vine and Dinnat, 2022].

Surface roughness is the primary effect in the case of the derivative, ∂TB/∂WS, which is the sensitivity of TB to a change in WS. In the absence of a closed form expression that covers the frequency range of interest, a hybrid model which is a mix of theory and experiment is adopted here [Le Vine and Dinnat, 2022]. In this hybrid, the dependence of TB on wind speed at 1.4 GHz is specified using the model developed by [Yin et al, 2016] for 1.4 GHz and validated for Aquarius and SMOS observations. This is extended to other frequencies using a two-scale scattering model [Dinnat et al, 2003] with the Durden-Vesecky spectrum multiplied by a factor of two and a cutoff frequency of ¼ the electromagnetic frequency (although the results are not very dependent on the cutoff [Dinnat et al, 2003]). The hybrid is obtained by normalizing the frequency dependence from the two-scale model to unity at 1.4 GHz and then multiplying by the Yin et al model [Yin et al, 2016] to give the amplitude and dependence on wind speed. An example is shown in Fig. 2. The left panel shows ∂TB/∂WS as a function of frequency for nadir (dashed) and 40 deg incidence; The right panel shows the sensitivity at nadir for several values of SST. As can be seen the sensitivity to WS increases with frequency and the change with frequency is relatively slow compared to the change of the sensitivity to SSS and SST in this frequency range. As can be seen in the right panel in Fig. 2, the sensitivity of TB to changes in WS is only weakly dependent on SST. Both panels in Fig 2 are for WS = 7 m/s, and at a given frequency the sensitivity increases with increased wind speed. The change in sensitivity is almost linear with wind speed for WS > 5 m/s (e.g. see Fig 11 in [Le Vine and Dinnat, 2020]).

To compute the STD of the error in the retrieved SST due to errors in the input parameters, ΔTB, ΔSSS and ΔWS, the expressions for ∂TB/∂SSS, ∂TB/∂SST and ∂TB/∂WS are substituted into

Eqn 2b. Since the errors in the input parameters are assumed to be zero mean, the mean of the error of the retrieved SST is zero. The square root of Eqn 2b, the STD of the retrieval error, σ_{SST}, will be used as the metric for performance of the retrieval. The process is straight forward but the outcome requires care because a null in $\partial TB/\partial SST$ in the frequency range of interest can result in a singularity and an undefined value for σ_{SST}. This does not happen when one applies the same approach to the retrieval of SSS [Le Vine and Dinnat, 2022]. Consequently, to illustrate the approach and put the more complex behavior in the case of SST in perspective, an example for the retrieval of SSS will be given first.

3.2 Retrieval of Salinity

The mathematics for the retrieval of salinity is the same as above but with SST replaced by SSS and vice-versa. The procedure is described in detail in [Le Vine and Dinnat, 2022] where it is shown that the standard deviation for the error in retrieved salinity is:

$$\sigma_{SSS} = \text{sqrt}\{<\Delta SSS^2>\} \quad (4a)$$

$$= \text{sqrt}\{[<\Delta TB^2> + (\partial TB/\partial SST)^2 <\Delta SST^2> + (\partial TB/\partial WS)^2 <\Delta WS^2>] / (\partial TB/\partial SSS)^2 \} \quad (4b)$$

Figure 3 is an example of σ_{SSS} obtained by substituting the sensitivities illustrated in Figs 1-2 into Eqn 4. The figure shows the STD of the error in retrieved salinity as a function of frequency for nadir (dashed), and at 40 deg incidence for horizontal polarization (red) and vertical polarization (blue). In this example SSS = 35 psu, WS = 7 m/s and the STD of errors in radiometer noise, SST and WS are 0.1K, 0.5 ºC and 0.5 m/s, respectively. The panel on the left is for warm water (SST = 20 ºC) and on the right for cold water (SST = 2 ºC). For example, for a measurement at 1 GHz in warm water at nadir (Fig 3; left, dashed curve) the STD of the retrieval

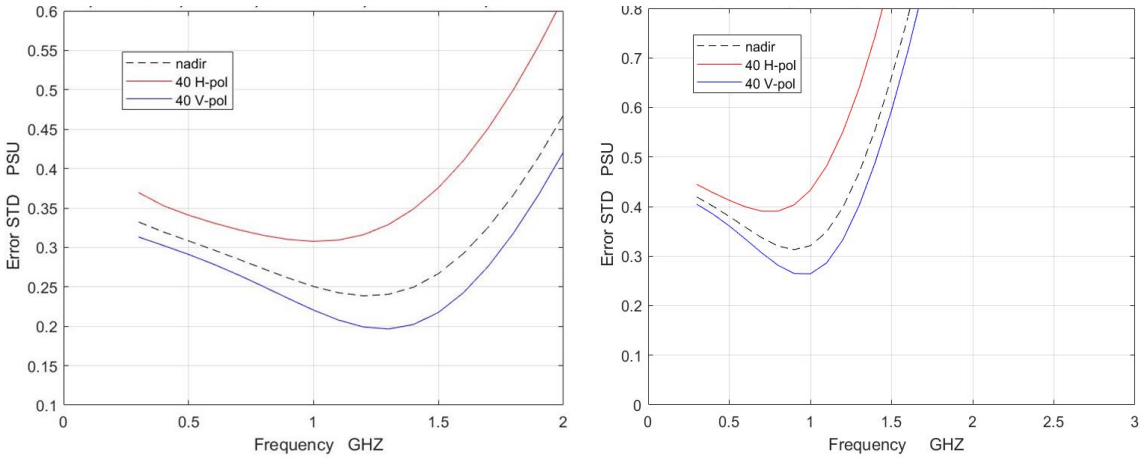

Figure 3: Standard deviation of salinity error as a function of frequency for (left) warm water (20 ºC) and (right) cold water (2 ºC). In both panels SSS = 35 psu, WS = 7 m/s and σ_{TB} = 0.1 K, σ_{SST} = 0.5 ºC and σ_{WS} = 0.5 m/s. The dashed curve is for nadir incidence and the solid curves for an incidence angle of 40 degrees (red for horizontal polarization and blue for vertical polarization).

error is about 0.25 psu. In cold water (Fig 3; right, dashed curve) a measurement at the same frequency would result in a retrieval error with an STD of a little more than 0.3 psu.

The U shape of the curves and location of the minimum is largely a consequence of the sensitivity to water temperature, ∂TB/∂SST, which has a null (zero) near 2 GHz for very warm water that shifts toward lower frequency as the temperature decreases and is close to 1 GHz for cold water (Fig. 1). At frequencies above the minimum in the error curve, the errors increase rapidly because the sensitivity to salinity, ∂TB/∂SSS, decreases rapidly at higher frequency. The errors for cold water (Fig. 3, right) are in general larger than for warm water, and even for a measurement at a frequency close to the minimum, the error in cold water is larger than in warm water.

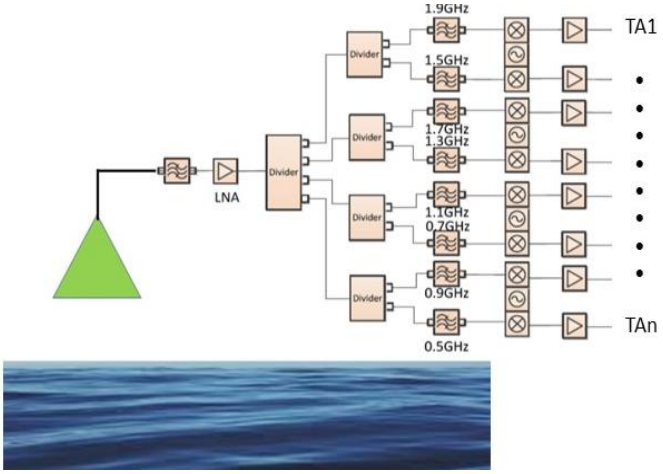

Figure 4: Wide bandwidth radiometer with multi-frequency channel output. The wide bandwidth input signal is divided into contiguous channels 100 MHz wide. The output is a set i = {1: n} of antenna temperatures TAi

An approach for improving accuracy is to make measurements at several frequencies including those near the peak in sensitivity to SSS (i.e. frequency below 1 GHz) and to do this simultaneously and then average the results. Using a range of frequencies is especially appealing since the shape of the curve and peak in the sensitivity move with temperature. In addition, this is not protected spectrum and although adequate signal is likely to be available in the ocean and sparsely populated land [Andrews et al, 2021] not all frequencies will be useful at all times. A radiometer system for making the multi-frequency measurement is illustrated in broad outline in Fig 4. The receiver divides the output from a wideband antenna system into several frequency bands which feed (in this application) independent retrieval algorithms tuned to each frequency. The individual salinity retrievals are then combined (e.g. averaged) to produce the final salinity product. Examples and options for the averaging can be found in [Le Vine and Dinnat, 2022]. In that analysis it is assumed that the radiometric noise in each frequency channel is independent and identically distributed. Also, it is assumed that for each measurement there is only one value of WS and SST for all channels (because the radiometer is looking at the same ocean during the measurement at all frequencies) and it is assumed that the error in WS and SST are independent

of each other and independent of the noise in radiometers. The STD of the retrieval using a simple, unweighted average is given by Eqn 17 in [Le Vine and Dinnat, 2022].

Figure 5 shows an example of the STD of the average using Eqn 17 in [Le Vine and Dinnat, 2022] in the case of a nadir look (dashed curve) and with measurements made at intervals of 100 MHz starting at 300 MHz. The dashed curves are the error STD for a measurement at a unique frequency as a function of frequency (same as in Fig. 3) and the circles represent the effect of averaging an increasing number of measurements. Starting at the left , the first circle represents the STD of a single measurement at 300 MHz (same as the dashed curve); The second circle is the average of the first measurement with a second measurement at 400 MHz; The third circle is the average of three measurements at 300, 400 and 500 MHz … and so on. Averaging improves the estimate of salinity as the number of measurements increase. However, eventually measurements with increasing error are added, and the STD of the average begins to get worse as measurements at higher frequencies with increasing error are added. The optimum upper limit depends on temperature, being about 2 GHz for warm water and 1.5 GHz for cold water. Also notice that in cold water the improvement from the multi-frequency retrieval is much greater than in warm water and using frequencies from 300 MHz to 1.5 GHz one obtains accuracies that are comparable to those in warm water.

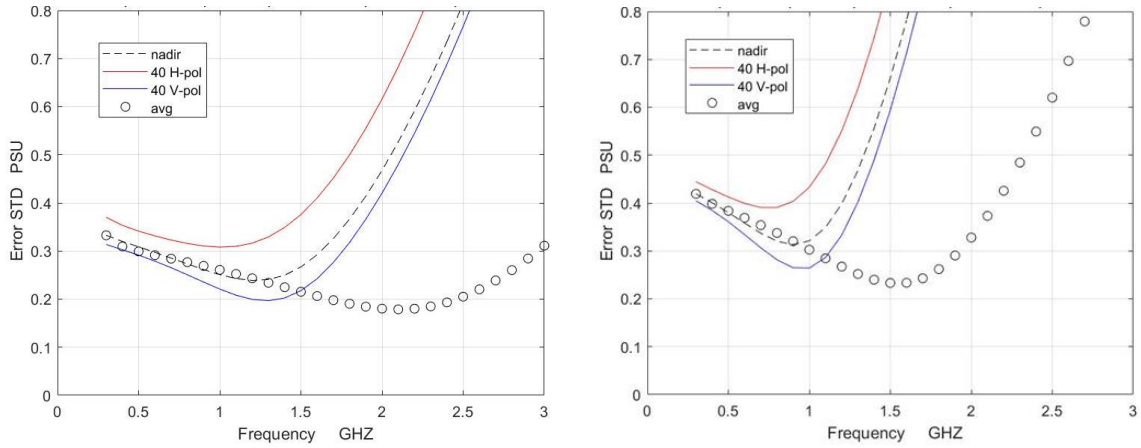

Figure 5: Error in retrieved SSS with increasing averaging for nadir incidence (dashed). The circles represent the average of an increasing number of frequency channels starting with a single measurement at 300 MHz and adding one channel every 100 MHz. Warm water (left; 20 ºC) and cold water (right; 2 ºC) with SSS = 35 psu, WS = 7 m/s, σ_{TB} = 0.1 K, σ_{SST} = 0.5 ºC and σ_{WS} = 0.5 m/s in both cases.

The same approach can be used to address the retrieval of SST. In principle (i.e., mathematically) one can use the same set of frequencies and radiometer hardware such as shown in Fig 4 to also retrieve SST. However, there is a problem when applying Eqn 2b: There is a null in the derivative ∂TB/∂SST in the frequency range 1-2 GHz (see Fig. 1) which results in a singularity where the mathematics does not apply. But, on either side of the singularity, Eqn 2b

is viable and a retrieval of SST is possible, and there appears to be enough useful spectrum to achieve a reasonable retrieval. This is shown in the examples below.

3.3 Retrieval of Sea Surface Temperature

The behavior of ∂TB/∂SSS and ∂TB/∂SST as a function of frequency and temperature (Fig. 1) is similar for frequencies below about 1 GHz: both have peaks that shift toward lower frequency as the temperature decreases. However, above 1 GHz the behavior is much different. The sensitivity to changes in SSS decreases monotonically toward zero and has decreased to half the peak value at 2.5 GHz for warm water and much less for cold water. The sensitivity to changes in water temperature, ∂TB/∂SST, also decreases rapidly with increasing frequency, but unlike ∂TB/∂SSS it goes through zero (in the vicinity of 1-2 GHz depending on temperature) and then increases to a maximum of positive sign at frequencies between 3-8 GHz. The frequency of the positive peak depends on temperature moving to higher frequency as temperature increases (e.g., Fig. 1; also see Figs. 6-7 in [Le Vine Dinnat, 2020]).

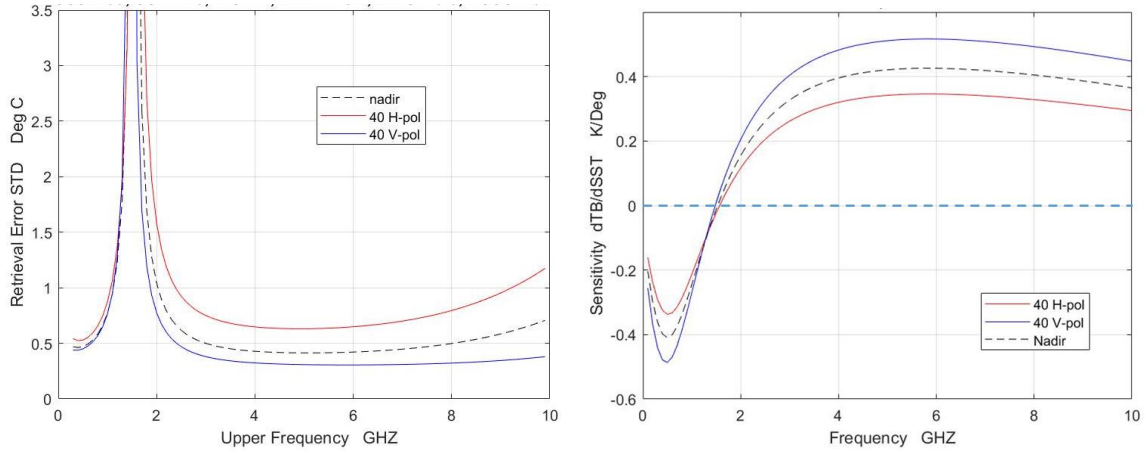

Figure 6 (Left): The STD of the error in retrieval of SST for the case of warm water (SST = 20 °C) with SSS = 35 psu and WS = 7 m/s with STD of errors in ancillary parameters: σ_{TB} = 0.1 K; σ_{SSS} = 0.2 psu and σ_{WS} = 0.5 m/s. (Right): The sensitivity ∂TB/∂SST for the same temperature and salinity. In both cases the dashed curve is for nadir and the solid curves for an incidence angle of 40 degrees.

The null in ∂TB/∂SST is a good thing in the retrieval of SSS because it means the sensitivity to errors in SSS are minimized. But, in the case of the retrieval of SST, this null is a problem because of ∂TB/∂SST appears in the denominator of Eqn 2b. As a result, the STD of the retrieval error, σ_{SST} , increases without limit at frequencies in the vicinity of the null. (Strictly speaking, the analysis doesn't apply at the singularity but can be used on either side). The consequence of this null is illustrated in Fig. 6. The results of substituting the sensitivities (Figs 1-2) into Eqn 2b is shown on the left for the case of warm water (SST = 20 °C) with SSS = 35 psu and WS = 7 m/s. The STD for the errors in TB and SSS and WS in this example are σ_{TB} = 0.1 K; σ_{SSS} = 0.2 psu and σ_{WS} = 0.5 m/s, respectively. On the right is a plot of ∂TB/∂SSS for the same temperature and salinity. In both cases the dashed curve is for nadir and the solid curves for an incidence angle of 40 degrees. Notice the transitions from negative to positive of ∂TB/∂SST near 1.5 GHz and the corresponding singularity in the calculations from Eqn 2b shown in the panel on the left. The frequency at which the null occurs is dependent on

polarization and for both polarizations depends on SST. The null moves toward lower frequency as the temperature decreases (e.g., Fig 1) and so does the singularity.

At frequencies between about 3 – 8 GHz, the STD of the retrieval error has a broad minimum. This corresponds roughly to the broad positive maximum in the sensitivity, $\partial TB/\partial SST$. Frequencies in this range are important in contemporary microwave remote sensing of SST using data from sensors such as AMSR-2 and Windsat [Gentemann et al, 2010; Gaiser et al, 2004; Le Vine 2019]. But at the frequencies under consideration here, the curve for the error STD is dominated by the singularity. At first glance it would seem impractical to try to retrieve SST at a frequency below 2 GHz. However, a closer look yields a more complex picture. Figure 7 and 8 show the STD of the retrieval error, σ_{SST}, in more detail for warm water and cold water, respectively. Only the results for the STD at nadir (dashed lines) are plotted to avoid clutter. In each figure, the panel on the right shows σ_{SST} as a function of frequency for frequencies below 5.0 GHz and in the panel on the left the frequency scale has been expanded to show the behavior at frequencies below the singularity in more detail. In the case of warm water (Fig. 7) the STD of the retrieval error after averaging frequencies less than about 900 MHz is about the same as at the conventional frequencies used in remote sensing of SST. In cold water (Fig. 8), σ_{SST} is actually better than for warm water for individual frequencies less than 700 MHz.

The circles in panels on the left in Figs 7-8 represent the effect of combining measurement from several frequencies. Each circle represents an additional term in the average and the final circle on the right in Figs 7-8 represents the average of 8 measurements covering the range 300 – 1000 MHz and spaced 100 MHz apart. A simple unweighted average was used (see Appendix B and [Le Vine and Dinnat, 2022] for details). In computing the average, it is assumed that for each measurement there is only one value of WS and SSS for all channels because the radiometer is looking at the same ocean during the measurement, and it is assumed that the error in WS and SSS are independent of each other and independent of the noise in radiometers. Finally, it is assumed that the noise in each radiometer is independent and statistically identical (i.e. independent, identically distributed random variables). In these examples the measurements are spaced 100 MHz apart; however, the results are not sensitive to the spacing [Le Vine and Dinnat, 2022].

As the frequency increases, averaging improves the estimate of SST compared to a single measurement at that frequency. For example, at 700 MHz in warm water (Fig 7), the STD of the error of a single measurement of SST (dashed curve) is larger than the average of the 5 measurements from 300 – 700 MHz. The improvement is larger in cold water (Fig 8) than in warm water. But, in the cases shown in Figs 7-8, the accuracy achieved with the average is only marginally better than with a single measurement at 300 MHz. This is because of the upward trajectory of the dashed curve (which gives the STD of the error at an individual frequency as a function of frequency); and it is in contrast to the impact of averaging in the case of the retrieval of SSS (Fig. 5) where averaging significantly improves the retrieval (e.g., averaging all the measurements from 0.3 – 1.5 GHz reduces the STD of a single measurement at 1.5 GHz from

320 0.6 psu to 0.25 psu). However, the improvement in the SST retrieval with averaging depends on
321 the sensitivity (noise level) of the radiometers as will be discussed below.

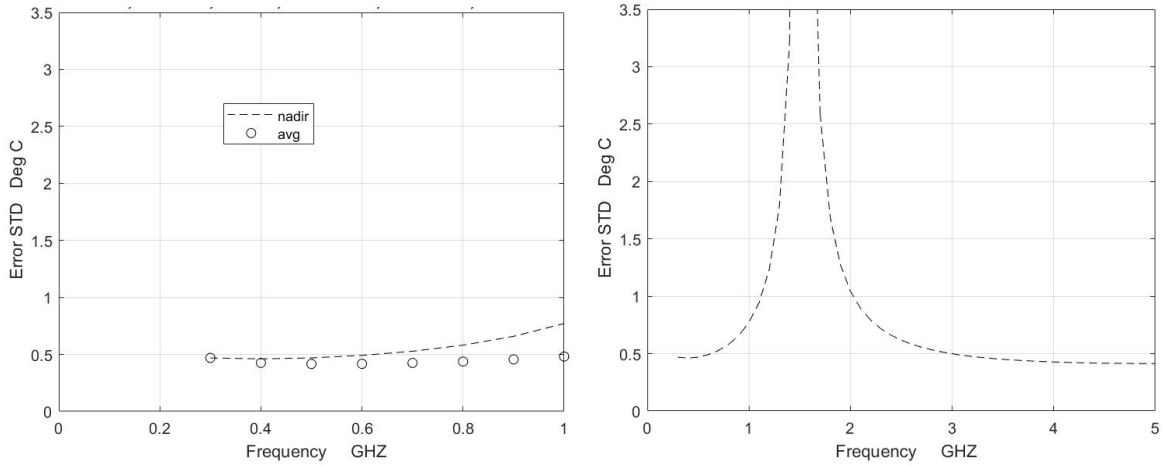

Figure 7. Standard deviation of the SST retrieval error for nadir incidence and SST = 20 ^{0}C, SSS = 35 psu, WS = 7 m/s, and σ_{TB} = 0.1 K; σ_{SSS} = 0.2 psu and σ_{WS} = 0.5 m/s. The panel at the right shows the STD with a frequency range up to 5 GHz and the panel on the left shows the behavior below 1 GHz with an expanded frequency scale. The dashed curves are the STD as a function of frequency and the circles are the average with increasing number of frequency channels starting at the left at 300 MHz moving to the right in increments of 100 MHz.

322

323

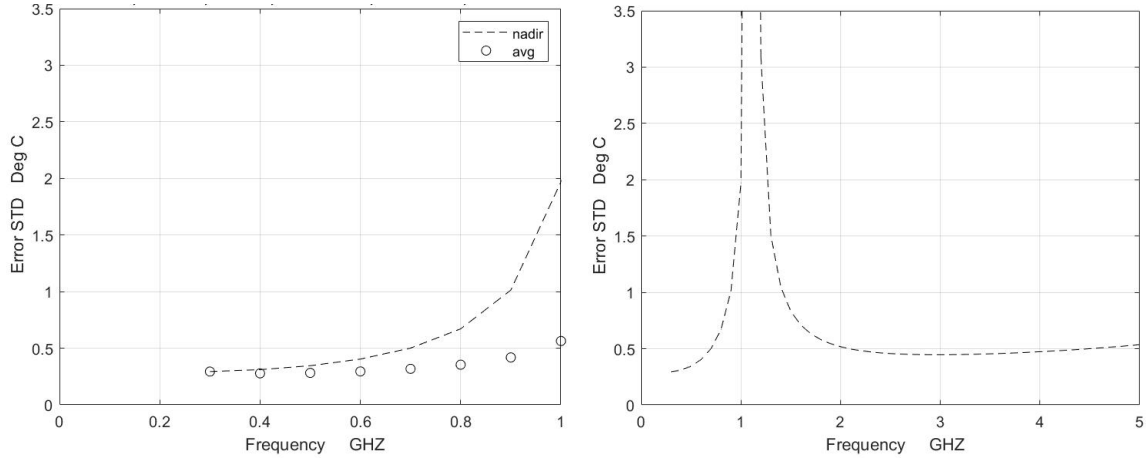

Figure 8: Standard deviation of the SST retrieval error for nadir incidence and SST = 2 ^{0}C, SSS = 35 psu, WS = 7 m/s, and σ_{TB} = 0.1 K; σ_{SSS} = 0.2 psu and σ_{WS} = 0.5 m/s. (Same as Fig 7 but for cold water.) The panel at the right shows a frequency range up to 5 GHz and the left panel shows the behavior below 1 GHz with an expanded frequency scale. The circles are the average with increasing number of frequency channels moving from left to right.

4 Discussion

4.1 Radiometric Noise

The error at any given frequency increases with an increase in the radiometric noise (e.g. radiometer resolution [Randa et al., 2008]). This is illustrated in Fig. 9 which shows the error STD for σ_{TB} = 0.1 K (black) and σ_{TB} = 0.3 K (red). In both cases, SST = 2 ºC with SSS = 35 psu, WS = 7 m/s and the error STD for the input SSS and WS are σ_{SSS} = 0.2 psu and σ_{WS} = 0.5 m/s, respectively. As above, the circles represent the average with increasing number of frequency channels starting with one channel at 300 MHz and adding one channel each 100 MHz moving from left to right.

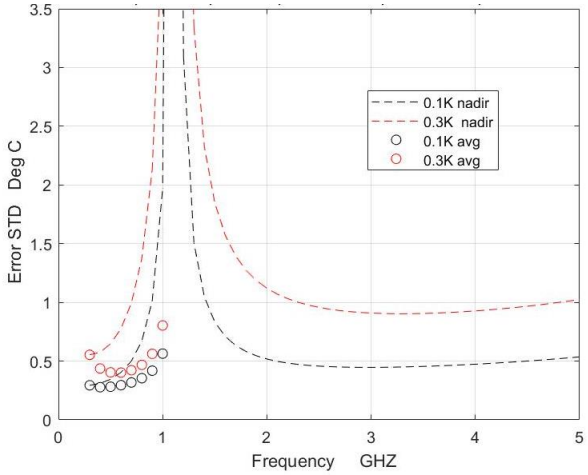

Figure 9: Effect of radiometric noise on SST retrieval error for σ_{TB} = 0.1 K (black) and σ_{TB} = 0.3 K (red). In both cases, SST = 2 ºC with SSS = 35 psu, WS = 7 m/s and the error STD for the input SSS and WS are σ_{SSS} = 0.2 psu and σ_{WS} = 0.5 m/s, respectively. The circles represent the average with increasing number of frequency channels starting with one channel at 300 MHz and adding one channel each 100 MHz moving from left to right.

It is clear from Fig. 9 that the error at an individual frequency (dashed curve) increases as σ_{TB} increases, and it is easy to see from Eqn 2b that this should be the case because the error increases directly with $\sigma^2_{TB} = \langle \Delta TB^2 \rangle$. This is true both for the low frequency regime below the singularity and, also above the singularity. Averaging has a significant impact on the error in the case of the larger σ_{TB} (red circles). In the unweighted average employed here (Appendix B), the contribution of radiometric noise decreases with the number, N, of frequency channels and in the case of uniformly spaced frequencies that contribution to the STD of the error decreases approximately as $1/\sqrt{N}$. In the case of the larger σ_{TB} the STD of the final (averaged) product decreases rapidly, and after averaging only a few measurements is comparable to the accuracy achieved with the lower σ_{TB} (black curve and circles). In the case of the higher radiometric noise (red circles) the averaged product is also better than would be achieved by a single measurement in the frequency range used for remote sensing SST (e.g. red curve at f > 3 GHz); and with the best combination (e.g. average of 4 frequency channels 300 - 600 MHz) is comparable to that obtained with the much lower

radiometric noise (black curve). But the impact of averaging depends on the relative contribution of the errors of the input parameters TB, SSS and WS. When σ_{TB} is dominant, then averaging yields a noticeable improvement. Averaging does not affect the errors in SSS and WS nearly as strongly because there is only one value of SSS and WS for each observation (scene) of the sensor and at some point these errors can dominate the final STD (see Eqn 3 in Appendix B). With a sufficiently accurate radiometer, little is to be gained with averaging, and using a single frequency (300 MHz or the lowest available) may be optimum.

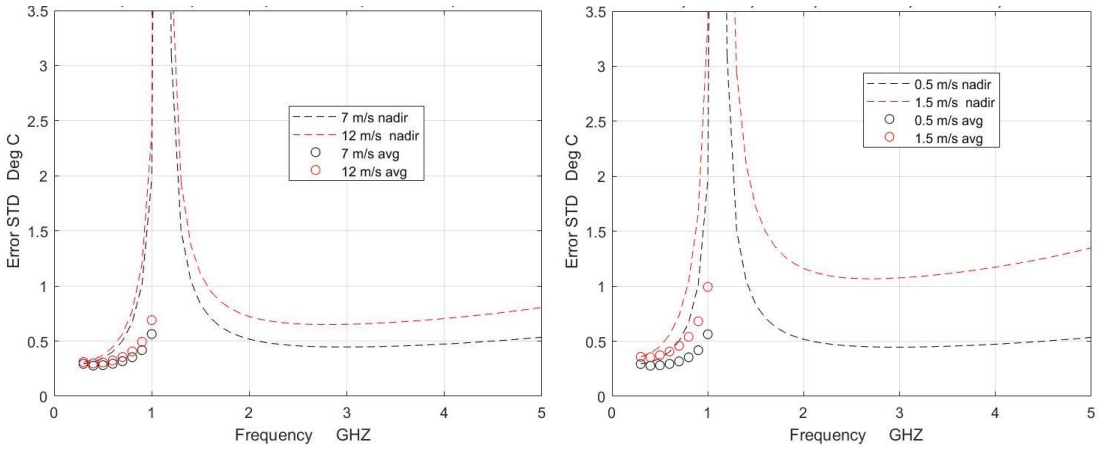

Figure 10: The effect of WS and the error in WS on the retrieval of SST. (Left): The effect of WS itself on the retrieval of SST with two cases, WS = 7 m/s (black) and WS = 12 m/s (red), and in both examples σ_{WS} = 0.5 m/s; (Right): The effect of error in WS with σWS = 0.5 m/s (black) and σWS = 1.5 m/s (red) and in both examples WS = 7 m/s. For both panels SST = 2 ºC with SSS = 35 psu, and the error STD for TB and SSS are σ_{TB} = 0.1 K and σ_{SSS} = 0.2 psu, respectively. The circles are the average with increasing number of frequency channels in steps of 100 MHz moving from left to right.

4.2 Wind Speed

Operating at low frequencies is an advantage when it comes to the effect of wind on the remote sensing of SST. The sensitivity of TB to changes in WS is lowest in the low frequency regime and increases with increasing frequency (Fig. 2). At WS = 7 m/s the increase is relatively rapid until about 10 GHz when ∂TB/∂WS tends to saturate at vertical polarization and continues to increase but at a slower rate at horizontal polarization; but above a few GHz the frequency dependence changes with wind speed (for example, see Figs 12-13 in [Le Vine and Dinnat, 2020]). Therefore remote sensing at frequencies below the singularity is less affected by WS than at higher frequencies. There are two parameters associated with WS that can affect the retrieval: WS itself and the error in the estimate of WS. These two effects are illustrated in Fig 10 which reports the STD of the error in the retrieved SST due to (left) the effect of WS and (right) the effect of the error in knowledge of the wind speed (i.e., σ_{WS}). For both left and right, SST = 2 ºC, SSS = 35 psu and the error STD for TB and SSS are σ_{TB} = 0.1 K and σ_{SSS} = 0.2 psu, respectively. The left panel shows the retrieval error for WS = 7 and 12 m/s and σ_{WS} = 0.5 m/s in both cases. There is a noticeably larger increase in the STD of the error in SST when WS increases at frequencies above the singularity than for frequencies below which is a reflection of the change in the dependence of

TB on WS with frequency (e.g., Fig 2). The retrieval using the average of multiple frequencies (circles) is only slightly impacted by the increase in WS using frequencies below about 800 MHz.

The dependence of the error in the retrieval of SST on the error in the estimate of WS is illustrated in the right panel of Fig. 10 which shows σ_{SST} for two cases: σ_{WS} = 0.5 m/s (black) and 1.5 m/s (red). In both cases WS = 7 m/s. The retrieval error increases with increased σ_{WS} and as before the increase is larger at frequencies above the singularity. The retrieval using the average over multiple frequencies also increases and averaging does not compensate for the increase in σ_{WS}. Averaging improves the retrieval compared to using a single frequency except for the lowest frequency (300 MHz) but as described above this is a function of radiometric sensitivity which is σ_{TB} = 0.1 K in these examples. Again, this is because there is only one WS and one error, ΔWS, for each set of measurements, and averaging does not have the advantage of reducing random noise in WS and SSS that it has in the case of radiometric noise (Section 4.1).

4.3 Dependence on Salinity

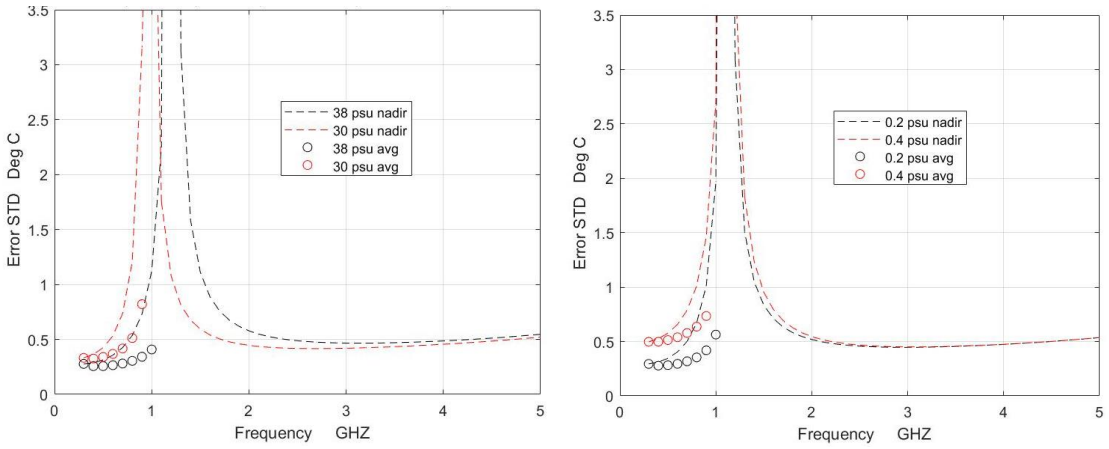

Figure 11: Effect of SSS on the error in retrieval of SST. Left: The effect of SSS with salinity values of SSS = 38 (black) and SSS = 30 psu (red) and σ_{SSS} = 0.2 psu. Right: Effect of error in SSS with values of σ_{SSS} = 0.2 (black) and 0.4 psu (red) and SSS = 35 psu. In all cases SST = 2 ºC and WS = 7 m/s and the error STD for TB and WS are σ_{TB} = 0.1 K and σ_{WS} = 0.5 m/s, respectively. The circles are the average with increasing number of frequency channels in steps of 100 MHz moving from left to right.

The error in the retrieval of SST depends strongly on salinity for frequency below 1 GHz. This is to be expected because this is the regime where the sensitivity of TB is strong for both changes in SST and SSS (e.g., Fig 1). This is illustrated in Fig 11 which shows the error, σ_{SST}, for SSS = 38 psu (black) and SSS = 30 psu (red) which are representative of the range encountered in the open ocean (e.g. Fig 11 in [Dinnat et al, 2019]). In both cases SST = 2 ºC, WS = 7 m/s and the error STD for TB, SSS and WS are σ_{TB} = 0.1 K, σ_{SSS} = 0.2 psu and σ_{WS} = 0.5 m/s, respectively. Cold water has been chosen for Fig 11 because the use of wideband sensing in the cryosphere is the focus of the analysis being done here. The cryosphere is also where a large range of values of SSS

are likely to be encountered, for example, due to freshwater outflow and melting ice. The effect of salinity is small at frequencies above the singularity and negligible in the regime where conventional remote sensing of SST is done (e.g. 6-7 GHz).

Salinity has two effects on the STD of the retrieval error (dashed curves) at lower frequencies. First, decreasing salinity (red curve) moves the singularity toward lower frequency. This can be seen by comparing the error at 38 psu (black dashed) to the error at 30 psu (red dashed). The location of the singularity is also temperature dependent and moves toward lower frequency as the temperature decreases. Low temperatures and low salinity combine to limit the frequency space available for retrieval of SST.

The retrieval error, σ_{SST}, also depends on the error in SSS. This is illustrated in the right hand panel in Fig 11 which shows the retrieval error for two cases: $\sigma_{SSS} = 0.2$ psu (black) and $\sigma_{SSS} = 0.4$ psu (red). In both cases SSS = 35 psu, SST = 2 ^{o}C, WS = 7 m/s and the error STD for TB and WS are $\sigma_{TB} = 0.1$ K and $\sigma_{WS} = 0.5$ m/s, respectively. As was the case with SSS itself, the impact of error in SSS is limited to the low frequency regime (below the singularity) where the sensitivity to changes in SSS is strong and is almost negligible at frequencies above a few GHz where the sensitivity is very small. Averaging in the case of moderate salinity (e.g. 35 psu) and low error in salinity (e.g., $\sigma_{SSS} = 0.2$ psu) might provide some improvement using the first few frequencies (e.g. black circles in left panel of Fig 11); however, the improvement is modest even in this case and with higher error a single measurement at the lowest frequency (e.g. 300 MHz) might be the best choice.

4.4 Statistics

The values of σ_{SST} and σ_{SSS} given here (i.e., Eqn 4b and B3) are the standard deviation of the error in the retrieval of SSS and SST. They are an indication of the variability (about the mean) in the outcome of a single look at the scene. But in a realistic scenario for remote sensing of the cryosphere there are likely to be several revisits. Microwave remote sensing of the cryosphere will most likely be done from low earth orbit with high inclination (i.e. a polar orbit) in which case there will be relatively frequent over passes over the same scene. The number will depend on the design of the sensor system (i.e., spacecraft orbit, spatial resolution and field of view of the sensor) but even with a non-scanning instrument one can expect several visits in a week for latitude above 65 degrees. Hence, there is likely some additional improvement that might be possible with averaging of these observations. This is another argument for retrieving SST because not relying on an ancillary source with longer updates may help insure the independence of the random variables representing the error in the repeat looks (e.g. if the revisit time is short compared to the update available from ancillary data).

5 Conclusion

In earlier work [Le Vine and Dinnat, 2022] it was shown that using a wide bandwidth radiometer such as shown in Fig. 4 has the potential to improve remote sensing of SSS in cold water where (i.e. high latitudes) improved accuracy is important to advance understanding of ocean circulation in the context of climate change. Analysis presented here suggests that with such a system it is also be possible to retrieve SST. A null in the sensitivity of brightness temperature to changes in

water temperature in this frequency range limits the frequencies available for remote sensing of SST. However, by restricting the measurements to frequencies below about 800 MHz, it may be possible to achieve a viable retrieval of SST and in cold water perhaps with accuracy as good as or better than using frequencies near C-band.

While a wide-band microwave radiometer operating at frequencies between 0.3 – 2 GHz probably would not work close to population centers where radiation from manmade sources would likely be an insurmountable problem, it might be feasible for high latitudes and the open ocean, especially given development of sophisticated detectors for RFI such as demonstrated by SMAP [Piepmeier et al., 2014; Johnson et al., 2016]. Furthermore, studies show that in remote regions where this application is likely to be important (i.e., the cryosphere), RFI is less of a problem than in populated parts of the globe and that frequency channels in this portion of the spectrum remain viable [Andrews et al, 2021].

Current work suggests that a wideband receiver system could retrieve both SSS and SST. Retrieving SST as part of the basic SSS retrieval algorithm offers the additional potential of having real time data to replace what is now SST obtained from other satellite measurements and interpolated in space and time. As pointed out in Section 4.3, an issue in the retrieval of SST is its dependence on SSS. However, the potential exists to retrieve both SSS and SST at each scene and perhaps improve both. Among the possibilities is a simple iterative approach, starting with a traditional retrieval of SSS using a best available ancillary value of SST. Then a retrieval of SST could be made using the retrieved SSS. A second retrieval of SSS would then be made but using the updated value of SST. The process would be repeated until the values of SST and SSS were stable. Another possibility is a two-parameter minimization of the difference between theory and observation using for example a maximum likelihood estimator with parameters SSS and SST and taking advantage of the frequency dependence of TB on SST and SSS over this frequency range to improve the estimate. In addition to SST and SST, it might be possible to include WS in such a minimization. Work along these lines is needed in the future to determine the true potential of retrieving SST and improving the accuracy of SSS in high latitudes and cold water.

In the case of the retrieval of SSS, the authors have shown that combining (e.g., averaging) measurements at multiple frequencies in the range of 0.3 – 1.5 MHz can improve accuracy compared to a measurement at a single frequency and yield accuracy better than with a single frequency at 1.4 GHz as is currently done, especially in cold water [Le Vine and Dinnat, 2022]. The authors entered this study assuming that averaging would most likely help in the retrieval of SST. It does help when the radiometric sensitivity is poor (Section 4.1). However, with a good radiometer the retrieval error is dominated by the error in WS and SSS and averaging produces modest if any improvement compared to a retrieval using the lowest frequency available. The best approach may be to retrieve SST at frequencies below the singularity using a dedicated frequency without averaging. However, the use of several frequencies is essential to applications in the cryosphere such as profiling ice sheet temperature [e.g., Johnson et al, 2021] which are likely to drive any future sensor and averaging is important for improving the retrieval of SSS in cold water [Le Vine and Dinnat, 2022]. Assuming that a selection of frequencies will be available, the retrieval of SST can be tuned to select the best frequency available (e.g., in the presence of RFI) or the retrieval could use an average of several frequencies to reduce noise, a choice which can be made depending on experience with the retrieval under the specifics of the sensor and scene. The

choice may also be determined when the optimum approach to retrieving both SSS and SST together is determined and whether the retrieval is over warm or cold water.

Finally, the analysis presented here ignores an important part of the retrieval process: Converting the output of the radiometer (antenna temperature, TA) into brightness temperature, TB, and the science product, SST. There are many parameters that must be taken into account in doing so; and unfortunately, many of these are frequency dependent and will vary from channel to channel. Some of them are: Radiometer calibration (e.g. gain and bias); Variation of the antenna pattern with frequency (which will also impact correction for land/ice contamination); Galactic background radiation; and atmospheric attenuation and emission. The analysis presented in the manuscript suggests that a retrieval is possible, but it doesn't solve the problem of actually obtaining an accurate retrieval.

Appendix A: Effect of Roughness on ∂TB/∂SST

Analysis is presented in this appendix to examine the assumption that the effect of roughness (i.e. wind driven waves) on the sensitivity ∂TB/∂SST is small enough to be neglected at the level of the approximation presented in the text above. Calculations are present at 1.4 GHz where the most accurate information on the effect of roughness is available. The calculations have been made using the model of Yin et al. [2016] which was developed for SMOS and is the basis for the hybrid model used here to compute the sensitivity ∂TB/∂WS (see Section 3.1).

It is common practice at L-band (i.e., in the retrieval algorithms of SMOS, Aquarius and SMAP) to write the brightness temperature of the ocean as the sum of the contribution from a flat surface (WS = 0) and a component due to roughness:

$$TB = TBflat + TBrough \quad \text{A1}$$

from which the sensitivity to changes in SST is:

$$\partial TB/\partial SST = \partial TBflat/\partial SST + \partial TBrough/\partial SST \quad \text{A2}$$

In these expressions ∂TBflat/∂SST is the sensitivity to SST due to an ideal flat surface (i.e., the sensitivity used in the text and shown in Fig 1) and ∂TBrough/∂SST is the change in the sensitivity due to ocean surface roughness. The Yin et al. [2016] model provides an expression for TBrough as a function of SST which can be differentiated (numerically) to yield ∂TBrough/∂SST. An example is shown in Fig A1.

Fig A1 shows ∂TBrough/∂SST as a function of WS computed using the model of Yin et al [2016] for the case of cold water (SST = 2^{o}C) and an incidence angle of 40 degrees. The panel on the right reports the absolute value of ∂TBrough/∂SST and the panel on the left reports the value relative to the sensitivity of the flat surface, specifically, the ratio [∂TBrough/∂SST] / [∂TBflat/∂SST] expressed in percent. The contribution due to roughness increases monotonically with WS and is a little larger at horizontal polarization than at vertical polarization. The contribution to the sensitivity is quite small but at 1.4 GHz the contribution from the flat surface is also small (e.g. Fig 1). The percentage change relative to the flat surface (left in Fig A1) can

be large at very high WS (e.g. about 15% at 20 m/s), but at WS typical of the ocean (e.g. 8 m/s) it is only 4%.

The calculations reported in Fig A1 were repeated using the model for the effect of roughness on TB developed for use in Aquarius (see Eqns 4-6 in [Meissner, Wentz, Ricciardulli, 2014] and Eqn 1 in [Meissner, Wentz, Le Vine, 2018]). The results from the Aquarius model are similar (e.g., monotonically increasing with WS and at horizontal polarization about 6 % at 8 m/s and 12 % at 20 m/s). The major difference of the Aquarius model calculation is that the values for vertical polarization are much lower at all WS (e.g. less than 2% at 8 m/s).

These calculations indicate that for most WS it is acceptable to neglect the effects of WS in computing the sensitivity to SST. However, the analysis only applies at 1.4 GHz and the application made here is primarily for frequencies lower than 1.4 GHz and as low as 300 MHz.

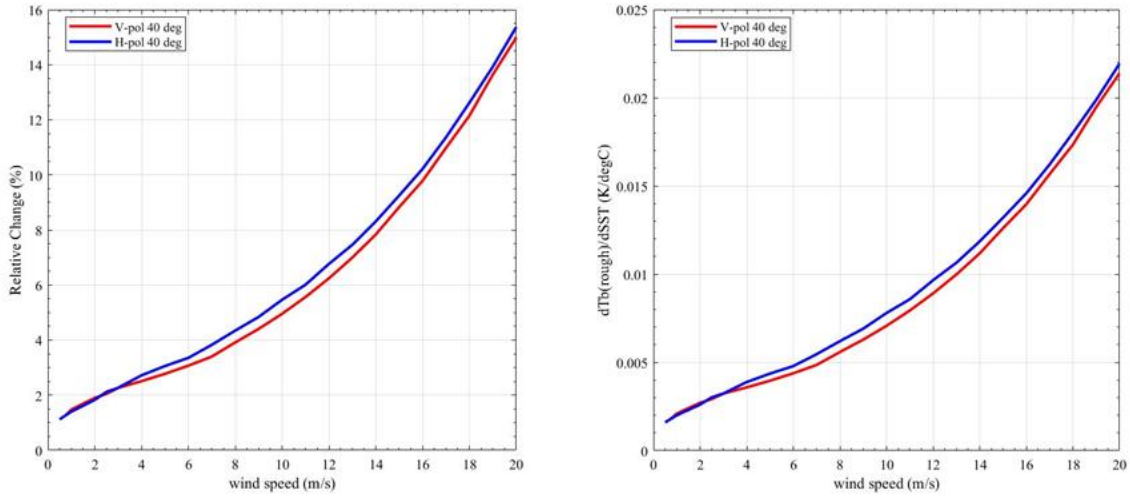

Figure A1. The change in sensitivity, $\partial TB_{rough}/\partial SST$, as a function of WS at 40 degree incidence for SST = 2°C and SSS = 35 psu. Left: the value of sensitivity relative to the value of a flat surface expressed in percent; Right: the absolute value of the sensitivity.

But the effect of roughness is expected to decrease with frequency and longer wavelength (e.g. Fig 2 in the main text); hence, these results most likely provide an upper bound for lower frequencies.

Appendix B: Averaging multi-frequency retrievals

In the multi-frequency measurement system envisioned in this manuscript (Fig 4), the receiver divides the output from a wideband antenna-detector system into several frequency bands which feed independent retrieval algorithms tuned to each frequency. The net effect is as if each frequency channel had its own, but identical, radiometer electronics and appropriate retrieval algorithm. It has been assumed that the system is ideal in the sense that it is calibrated with no bias or systematic errors. The SST at the output of the retrieval algorithm at each frequency are

then combined to produce the final SST product. Because of the different frequencies, the retrieval algorithm will not necessarily be the same for each channel (e.g. Faraday rotation varies rapidly with frequency in this frequency range). Consequently, it is not practical to average the retrieved TA or even TB at the surface before retrieval.

In this manuscript, a simple unweighted average is employed as an example. It has been assumed that the frequency channels are contiguous and uniformly spaced in increments of 100 MHz over the frequency interval employed (e.g. 0.3 – 1.0 GHz). The issue of irregularly spaced channels and/or frequency channels lost to RFI is not considered. The issue of finding an optimum weighting of the channels to improve the final retrieval also is not addressed here (see [Le Vine and Dinnat, 2022] for a discussion of this point). A brief outline of the analysis leading to the STD of the final averaged retrieval is outlined the following paragraphs.

The goal is to obtain an estimate of the standard deviation of the error, ΔSST, in the final retrieval as a function of the radiometer noise, ΔTB, and the error in the ancillary value of wind speed, ΔWS, and sea surface salinity, ΔSSS. Letting ΔSSTi represent the error in the retrieval at each channel, the error ΔSST after averaging the retrieval from each individual frequency is:

$$\Delta SST = (1/N)\, \Sigma_N\, (\Delta SSTi) \qquad (B1)$$

where the Σ_N is the sum over the N frequency channels. Only random errors are examined. Issues such as calibration and systematic errors in the retrieval algorithm or ancillary data are not included. Hence, ΔSST and the random variables ΔTB, ΔSSS and ΔWS are zero mean. Using Eqn 1b and assuming that ΔSSS and ΔWS are the same for all frequencies, Eqn B1can be written in the form:

$$\Delta SST = (1/N)\, \{\, \Sigma_N\, (Ai\, \Delta TBi) + \Sigma_N\, (Ai\, \partial TB/\partial SSSi)\, \Delta SSS + \Sigma_N\, (Ai\, \partial TB/\partial WSi)\, \Delta WS \,\} \qquad (B2)$$

It will be assumed that the radiometric noise, ΔTBi, in each frequency channel is independent and identically distributed. Also, it is assumed that for each measurement there is only one value of WS and SST for all channels (since they are looking at the same ocean during the measurement) and consequently only one value of ΔSSS and ΔWS. Furthermore, it is assumed that ΔSSS and ΔWS are independent of each other and independent of the noise in radiometers. The mean error $\langle \Delta SSS \rangle = 0$ (by assumption) and standard deviation of the error, σ_{SST}, of the error is [Le Vine and Dinnat, 2022]:

$$\boldsymbol{\sigma}_{SST} = \mathrm{sqrt}\{\Sigma_N\, (Ai^2)\, \boldsymbol{\sigma}^2_{TB} + [\Sigma_N\, (Ai\, \partial TB/\partial SSSi)]^2\, \boldsymbol{\sigma}^2_{SSS} + [\Sigma_N\, (Ai\, \partial TB/\partial WSi)]^2\, \boldsymbol{\sigma}^2_{WS}\} / N \qquad (B3)$$

where σ_{SST}, σ_{WS} and σ_{TB} are the STD of the error in SST, WS and the radiometric noise, respectively, and Ai is the inverse of the sensitivity of TB to SST in the i-th frequency channel: $Ai = (\partial TB/\partial SSTi)^{-1}$.

The circles in figures 7-11 are computed using Equation B3 with increasing number of frequencies, N, starting with N = 1 (corresponding to a single measurement at 300 MHz) and then increasing in increments of 100 MHz.

There are ways other than a simple, unweighted average to combine the measurements. For example, an optimum estimate for samples with independent Gaussian noise is to weight the average by the standard deviation [Yin et al, 2012]. Examples, of using this approach can be found in Appendix D of [Le Vine and Dinnat, 2022]. Using as weights the STD computed with Eqn 2b (the dashed curves in Figs 7-11) tends to flatten the unweighted average (circles in these figures) as more measurements closer to the singularity are included. However, this approach is probably overly optimistic in the context of the analysis done here because these STDs are ideal (from theory) and don't represent the full uncertainty in a real world retrieval.

Acknowledgments

Part of this research was funded by the National Aeronautics and Space Administration, grant number 80NSSC18K1443.

Date Availability Statement

No data was used in the analysis presented here.

References

Andrews, M. .J., J.T. Johnson, Marco Brogioni, Giovanni Macelloni, and Kenneth C. Jezek, 2021, Properties of the 500–2000-MHz RFI Environment Observed in High-Latitude Airborne Radiometer Measurements, *IEEE Trans. Geosci. Remote Sens.*, 2021 early access, doi 10.1109/TGRS.2021.3090945

Bindlish, R, S. Chan, A. Colliander, Y. Kerr and T.J. Jackson, 2019, Integrated SMAP and SMOS Soil Moisturre Observations, Proc. IEEE Internat. Geosci. and Remote Sensing Symposium (IGARSS) 2019, pp 5379, July, Yokohama, Japan.

Boutin, J., J. Vergely, E. P. Dinnat, P. Waldteufel, F. D'Amico, N. Reul, A. Supply and C. Thouvenin-Masson, 2021, Correcting Sea Surface Temperature Spurious Effects in Salinity Retrieved From Spaceborne L-Band Radiometer Measurements, IEEE Trans. Geosci. Remote Sens., Vol. 59, No. 9, Sept, 2021 doi: 10.1109/TGRS.2020.3030488

Chan, S., Bindlish, R., O'Neill, P., Jackson, T., Njoku, E., Dunbar, S., Chaubell, J., Piepmeier, J., Yueh, S., Entekhabi, D., Colliander, A., Chen, F., Cosh, M., Caldwell, T., Walker, J., Berg, A., McNairn, H., Thibeault, M., Martínez-Fernández, J., Uldall, F., Seyfried, M., Bosch, D., Starks, P., Holifield Collins, C., Prueger, J., van der Velde, R., Asanuma, J., Palecki, M., Small, E., Zreda, M., Calvet, J.-C., Crow, W., Kerr, Y., 2018. Development and Assessment of the SMAP Enhanced Passive Soil Moisture Product. Remote Sensing of Environment. 204, 931-941, doi:10.1016/j.rse.2017.08.025.

de Matthaeis, P., D.M. Le Vine, Y. Soldo, A. Llorente, 2021, Study of a Strong L-Band RFI Source, IEEE Journal Selected Topics in Applied Earth Observations and Remote Sensing. Early access; DOI 10.1109/JSTARS.2021.3104264

Dinnat, E.P.; Le Vine, D.M.; Boutin, J.; Meissner, T.; Lagerloef, G., 2019, Remote Sensing of Sea Surface Salinity: Comparison of Satellite and In Situ Observations and Impact of Retrieval Parameters. Remote Sens. 2019, 11, 750 doi:10.3390/rs11070750.

Dinnat, E. P., J. Boutin, G. Caudal, and J. Etcheto, 2003, Issues concerning the sea emissivity modeling at L band for retrieving surface salinity, Radio Sci., vol. 38, no. 4, p. 8060, 2003, doi: 10.1029/2002RS002637.

Duncan, B. N., Ott, L. E., Abshire, J. B., Brucker, L., Carroll, M. L., Carton, J., et al., 2020, Space-Based Observations for Understanding Changes in the Arctic-Boreal Zone. *Reviews of Geophysics*, *58*(1). https://doi.org/10.1029/2019RG000652

Entekhabi, D.; Yueh, S.; O'Neill, P. E. and Kellogg, K. H., 2014, SMAP Handbook. Pasadena, CA, USA: Jet Propulsion Laboratory, Jul. 2014.

Entekhabi, D., Njoku, E.G., O'Neill, P., Kellogg, K., Crow, W., Edelstein, W., Entin, J., Goodman, S., Jackson, T.J., Johnson, J., Kimball, J., Peipmeier, J., Koster, R., McDonald, K., Moghaddam, M., Moran, S., Reichle, R., Shi, J., Spencer, M., Thurman, S., 2010. The soil moisture active and passive (SMAP) mission. Proc. IEEE. 98, 704-716.

Gaiser, P. et al, 2004, The WindSat space borne polarimetric microwave radiometer: sensor description and early orbit performance, IEEE Trans. on Geosci. and Remote Sensing, 42(11), pp. 2347-2361, doi: 10.1109/TGRS.2004.836867.

Gentemann, C. L., and Hilburn, K. A. (2015). In situ validation of sea surface temperatures from the GCOM-W1 AMSR2 RSS calibrated brightness temperatures. Journal of Geophysical Research: Oceans, 120, 3567– 3585. https://doi.org/10.1002/2014JC010574.

Gentemann, C.L., T. Meissner and F. J. Wentz, "Accuracy of Satellite Sea Surface Temperatures at 7 and 11 GHz," in IEEE Transactions on Geoscience and Remote Sensing, vol. 48, no. 3, pp. 1009-1018, March 2010, doi: 10.1109/TGRS.2009.2030322.

Kao, H.; Lagerloef, G.; Lee, T.; Melnichenko, O.; Meissner, T.; Hacker, P., 2018, Assessment of Aquarius Sea Surface Salinity, Remote Sens. 2018, 10(9), 1341 doi.org/10.3390/rs10091341.

Kerr, Y.H., Waldteufel, P.;Wigneron, J.-P.; Delwart, S.; Cabot, F.; Boutin, J.; Escorihuela, M.-J.; Font, J.; Reul, N.; Gruhier, C.; Juglea, S.E., Drinkwater, M.R., Hahne, A., Martin-Neira, M., Mecklengurg, S., 2010. The SMOS Mission: New Tool for Monitoring Key Elements of the Global Water Cycle Proc. IEEE 2010, 98, 666–687.

Klein, L. A. and C. T. Swift, 1977, An improved model for the dielectric constant of sea water at microwave frequencies, IEEE Trans. Ant. Prop., 1977, AP-25, pp. 104-111.

Jezek, K. et al., 2019, Remote sensing of sea ice thickness and salinity with 0.5-2GHz microwave radiometry, IEEE Trans. Geosci. Remote Sens., vol. 57, no. 11, pp. 8672–8684, Nov. 2019. doi: 10.1109/TGRS.2019.2922163

Johnson, J.T. et al., 2016, The cubesat radiometer radio frequency interference technology validation (CubeRRT) mission, in Proc. IEEE Int. Geosci. Remote Sens. Symp., 2016, pp. 299–301.

Johnson, J.T. et al, 2021, Microwave Radiometry at Frequencies From 500 to 1400 MHz: An Emerging Technology for Earth Observations, IEEE JSTARS, 2021, Vol 14, 4894-49140. doi 10.1109/JSTARS.2021.3073286

Le Vine, D.M. and E. Dinnat, 2022, Sensitivity of Wide Bandwidth Radiometer for Remote Sensing of Ocean Salinity, IEEE Trans. Geoscience and Remote Sensing, Vol 60, 5301517, 2022; doi: 10.1109/TGRS.2021.3101962

Le Vine D.M. and Dinnat, E., 2020, The Multifrequency Future for Remote Sensing of Sea Surface Salinity from Space, Remote Sens. 2020, 12, 1381; doi:10.3390/rs12091381.

Le Vine, D. M., 2019, RFI and Remote Sensing of the Earth from Space, Journal of Astronomical Instrumentation, Vol. 8, No. 1 (2019) 1940001 (13 pages) doi: 10.1142/S2251171719400014

Meissner, Thomas, Frank J. Wentz and David M. Le Vine, 2018, The Salinity Retrieval Algorithms for the NASA Aquarius Version 5 and SMAP Version 3 Releases, Remote Sens. 2018, 10, 1121; doi:10.3390/rs10071121

Meissner, Thomas, Frank J. Wentz and Lucrezia Ricciardulli, 2014, The emission and scattering of L-band microwave radiation from rough ocean surfaces and wind speed measurements from the Aquarius sensor, J. Geophys. Res. Oceans, 119, 6499–6522, doi:10.1002/2014JC009837.

Meissner, T. and F. Wentz, 2012, "The emissivity of the ocean surface between 6 and 90 GHz over a large range of wind speeds and earth incident angles", IEEE Trans. Geosci. Remote Sens. vol: 50, no. 8, pp. 3004-3026, 2012, doi:10.1109/TGRS.2011.2179662.

Meissner, T. and F. J.Wentz, 2004, "The complex dielectric constant of pure and sea water from microwave satellite observations", IEEE Trans. Geosci. Remote Sens., vol. 42, no. 9, pp. 1836–1849, doi: 10.1109/TGRS.2004.831888

Nielsen-Englyst, P.; L. Høyer, J.; Toudal Pedersen, L.; L. Gentemann, C.; Alerskans, E.; Block, T.; Donlon, C. Optimal Estimation of Sea Surface Temperature from AMSR-E. Remote Sens. 2018, 10, 229. https://doi.org/10.3390/rs10020229.

Pearson et al, 2019, "Sea Surface Temperature in Global Analyses: Gains from the Copernicus Imaging Microwave Radiometer", Remote Sens. 2019, 11, 2362; doi:10.3390/rs11202362

Piepmeier, J. R., et al., 2014, "Radio-frequency interference mitigation for the soil moisture active passive microwave radiometer," IEEE Trans. Geosci. Remote Sens., vol. 52, no. 1, pp. 761–775, Jan. 2014.

Rahmstorf, S. , 2006 , Thermohaline Ocean Circulation, Available online: https://courses.seas.harvard.edu/climate/eli/Courses/EPS281r/Sources/Thermohaline-circulation/1-Rahmstorf_EQS_2006.pdf (Also see Encyclopedia of Quaternary Science, 2013, Page:737-747).

Randa, J. et al, 2008, Recommended Terminology for Microwave Radiometry, Gaithersburg, MA, USA: National Institutes of Standards and Technology, NIST TN 1551, 2008.

Vinogradova, N. et al, 2019, Satellite Salinity Observing System: Recent Discoveries and the Way Forward, Frontiers in Marine Science, Vol 6, May, 2019, doi: 10.3389/fmars.2019.0024

Yardim, C. , *et al.*, 2022, "Greenland ice sheet subsurface temperature estimation using ultra-wideband microwave radiometry," *IEEE Trans. Geosci.Remote Sens.*, Vol 60, pp. 1-12 doi: 10.1109/TGRS.2020.3043954.

Yin, X., J. Boutin, E. Dinnat, Q. Song, and A. Martin, 2016, "Roughness and foam signature on SMOS-MIRAS brightness temperatures: A semi theoretical approach," Remote Sens. Environ., vol. 180, pp. 221–233, Jul. 2016.

Yin, X., J. Boutin and P. Spurgeon, First Assessment of SMOS Data Over Open Ocean: Part I—Pacific Ocean, IEEE Trans. Geosci. and Remote Sensing, 50(5), pp.1648-1641, May, 2012; doi: 10.1109/TGRS.2012.2188407

Zhou, Y., R. H. Lang, E. P. Dinnat and D. M. Le Vine, 2021, Seawater Debye Model Function at L-Band and Its Impact on Salinity Retrieval from Aquarius Satellite Data, *IEEE Trans. Geosci. Remote Sens.*, Vol. 59, No. 10, Oct. 2021 DOI 10.1109/TGRS.2020.3045771